Research Square

Preprints are preliminary reports that have not undergone peer review.
They should not be considered conclusive, used to inform clinical practice,
or referenced by the media as validated information.

A silver-containing ZnO/ZIF-8 composite: antibacterial activity and wound repair in an MRSA-inoculated rat model

Hang Xiao

xh871024@126.com

Shenyang Medical College

Hongbin Zhang

Liaoning University of Traditional Chinese Medicine

Zheng Xiang

Liaoning University

Jia Wang

Liaoning University

Fangli Yang

Shenyang Medical College

Research Article

Keywords: ZIF-8, zinc oxide, silver, antibacterial materials, infected wounds

Posted Date: November 20th, 2026

DOI: https://doi.org/10.21203/rs.3.rs-11642482/v1

License: This work is licensed under a Creative Commons Attribution 4.0 International License.
Read Full License

Additional Declarations: No competing interests reported.

A silver-containing ZnO/ZIF-8 composite: antibacterial activity and wound repair in an MRSA-inoculated rat model

Hang Xiao[1†*], Hongbin Zhang[2†], Zheng Xiang[3], Jia Wang[3], Fangli Yang[1]

[1] Basic Medical Science, Shenyang Medical College, Shenyang 113004, China

[2] School of Pharmacy, Liaoning University of Traditional Chinese Medicine, Dalian 116600, China

[3] School of Pharmaceutical Science, Liaoning University, Shenyang 110000, China

[*]Corresponding author: Hang Xiao

Email address: xh871024@126.com

[†]These authors contributed equally to this work.

Abstract

Silver-containing composites are being investigated for the local treatment of infected wounds. This study examined the material characteristics, antibacterial activity, and wound-healing effects of a silver-containing ZnO/ZIF-8 composite (ZAZ) prepared by treating ZIF-8 with silver nitrate. The material was characterized using electron microscopy, X-ray diffraction, elemental mapping, X-ray photoelectron spectroscopy, and infrared spectroscopy. Zinc and silver concentrations were measured in filtered saline suspensions after incubation. Antibacterial activity against *Escherichia coli*, *Staphylococcus aureus*, and methicillin-resistant *S. aureus* (MRSA) was assessed using plate culture and broth-based assays. Wound closure and tissue morphology were evaluated in MRSA-inoculated rat skin wounds with clinical signs of infection. Characterization supported the presence of ZIF-8, ZnO-related structures, and silver in the composite. No visible colonies were observed on the displayed ZAZ-treated plates under the assay conditions, whereas colonies remained visible in the ZIF-8 and ZnO groups. Day-14 wound closure was reported as 92.04% in the ZAZ group and 72.61% in the control group. Pathological section staining results show that this material can promote epidermal regeneration and ordered collagen deposition. Safety assessment confirms that it has no significant toxicity to metabolic organs. This study developed a ZnO@Ag-ZIF-8 nanoparticle based on the synergistic effect of bimetallic ions, which shows significant advantages in antibacterial properties and wound healing. This study offers new ideas for developing novel antibacterial materials and provides feasible solutions to the problem of antibiotic resistance.

Keywords: ZIF-8; zinc oxide; silver; antibacterial materials; infected wounds

1 Introduction

Infected wounds are a major challenge in the field of wound treatment, and can lead to delayed wound healing, increased morbidity, and potential complications [1]. The presence of microorganisms can disrupt the delicate balance of the wound microenvironment, hinder the healing process, and contribute to the formation of chronic wounds. Wound healing is a complex biological process that usually includes hemostasis and coagulation, inflammation, the formation of blood vessels and granulation tissue, as well as reconstruction and scar formation [2]. These stages often intersect and overlap with each other and are affected by a variety of factors [3]. Bacterial infection can interfere with all stages of the healing process and delay the healing rate of wounds. Wound infection usually leads to increased inflammation, prevents the formation of granulation tissue, inhibits fibrosis and the spread of infection [4]. After bacterial infection of the wound, the initially released white blood cells and inflammatory mediators increase, leading to a sustained inflammatory response and aggravated tissue damage. Bacterial invasion can also affect cell proliferation, interfere with the formation of blood vessels and granulation tissue in the wound, and delay wound filling. Bacteria also aggravate scar formation by affecting the process of collagen formation and fibrosis in the wound. Current research shows that the formation of biofilms and microbial communities encapsulated in a protective matrix further exacerbates wound infection and increases the difficulty of treatment [5]. Therefore, timely administration of antibacterial treatment and elimination of pathogens are the keys to promoting the healing of infected wounds. Hence, selecting appropriate wound dressings with antibacterial properties can help create an environment conducive to healing while reducing the microbial burden [6]. The emerging fields of bioactive materials and biomaterial-based therapies offer promising prospects for the management of infected wounds. However, the emergence of antibiotic-resistant bacteria poses challenges to the effective treatment of wound infections. Antibiotic resistance is a serious problem in wound care, as it hinders the healing process and causes unforeseen complications, thereby increasing mortality and morbidity [7]. Antimicrobial resistance remains a substantial global health challenge, and recent analyses demonstrate its continuing burden across bacterial pathogens [8-12]. Infected skin wounds provide a setting in which local bacterial control must be balanced against preservation of tissue repair. Materials intended for wound contact therefore require evaluation beyond bacterial inhibition alone: their composition, behavior in biological media, and effects on the surrounding tissue are relevant to their potential use.

Metal-organic framework materials (MOFs) have garnered significant attention in this context because of their intriguing properties and nanoscale dimensions, which provide novel approaches for wound healing. MOFs are a class of nanomaterials with highly porous crystalline structures formed by the coordination of organic ligands with metal ions. Due to their low toxicity, excellent biocompatibility, and high loading capacity, MOFs find broad applications in biomedicine, including drug delivery, bioimaging, biosensing, and antibacterial applications [13-15]. In recent years, as the range of MOF materials has continued to expand, they have demonstrated promising therapeutic efficacy and broad application prospects in the field of antibacterial agents [16, 17]. The unique physicochemical properties, morphological structures, and catalytic activity of MOFs underpin their widespread use in antibacterial applications [18-20].

In recent years, the potential of MOFs in antibacterial applications has been extensively explored. In particular, their antibacterial efficacy can be significantly enhanced by introducing metal ions with known antibacterial properties, such as zinc ions (Zn^{2+}) and silver ions (Ag^{+}) [21-23]. Zn^{2+} and Ag^{+} have long been renowned for their antibacterial effects [24, 25]. Zn^{2+} are essential for a variety of biological processes and have been shown to disrupt bacterial cell membranes and inhibit enzyme activity. Ag^{+}, by contrast, are characterized by their broad-spectrum antibacterial activity; they can penetrate bacterial cell walls and interfere with DNA replication and protein synthesis. Integrating these two metal ions into a single framework may further enhance their antibacterial efficacy through synergistic effects. Based on this approach, this study developed a novel bimetallic MOF-ZnO@Ag-ZIF-8 nanoparticles (ZAZ NPs) which combines the antibacterial properties of zinc and silver ions and is designed to provide an efficient and safe antibacterial agent for combating antibiotic-resistant bacterial infections.

In this study, microcatalytic technology was employed to convert Zn^{2+} on the surface of ZIF-8 into ZnO while simultaneously doping it with Ag to enhance the bacteriostatic performance of ZIF-8. A novel bimetallic MOF material-ZnO@Ag-ZIF-8 nanoparticles (ZAZ NPs) was designed and synthesized. In vitro experiments were conducted to evaluate the broad-spectrum antibacterial activity of this material against Staphylococcus aureus, Escherichia coli, and methicillin-resistant Staphylococcus aureus. Additionally, a full-thickness skin defect model in rats infected with MRSA was established to assess the material's antibacterial and wound-healing efficacy.

2 Materials and methods

2.1 Materials and bacterial strains

Zinc nitrate hexahydrate and 2-methylimidazole were obtained from Shanghai Macklin Biochemical, and silver nitrate was obtained from Nanjing Chemical Reagent. Methanol, saline, LB broth, nutrient agar, and tryptic soy agar were used as described below. *Escherichia coli* ATCC 8739, *Staphylococcus aureus* ATCC 6538, and MRSA ATCC 43300 were listed as supplied by Shanghai Biofeng. SD rats were listed as supplied by Liaoning Changsheng Biotechnology. The ZnO comparator was included in antibacterial testing.

2.2 Preparation of ZIF-8 and ZAZ

Zinc nitrate hexahydrate (10 mmol) was dissolved in methanol (100 mL) and stirred for 10 min. A methanolic solution containing 40 mmol 2-methylimidazole in 100 mL was added slowly, followed by stirring at room temperature for 24 h. The product was collected by centrifugation at the reported speed of 5000 rpm for 5 min and dried at 70°C. For the subsequent treatment, 0.68 g $AgNO_3$ was dissolved in a methanol/water medium, and 1 g ZIF-8 was added. After stirring for 1 h, the product was collected by centrifugation at 5000 rpm for 5 min and dried overnight at 70°C.

2.3 Material characterization and elemental measurements

SEM and TEM were used to examine morphology and lattice features. XRD was performed using Cu Kα radiation with a reported wavelength of 1.5406 Å over $2\theta = 5–50°$. Elemental distributions were examined by EDS, and surface composition was investigated using XPS. FTIR spectra were used to compare vibrational features before and after treatment. The listed instruments included an SU-8010 SEM, Talos F200X TEM, XRD-6100 diffractometer, ESCALAB 250Xi XPS system, and Nicolet iS50 FTIR spectrometer.

For elemental measurements, 7 mg ZAZ was dispersed in 100 mL saline and incubated at 37°C. Aliquots of 10 mL were taken at 2, 4, 8, and 24 h, centrifuged at 5000 rpm for 3 min, filtered through a 0.22 μm membrane, and digested with aqua regia before analysis using an Agilent 5110 ICP-OES instrument.

2.4 Plate-based antibacterial assay

Bacteria were cultured in LB broth at 37°C. The study compared saline control, ZAZ, ZIF-8, and ZnO groups after 4 h of co-incubation. According to the tabulated preparation scheme, 100 μL bacterial suspension at 10^7 CFU/mL was combined with material suspension

and saline to a total volume of 1 mL. Addition of 125 or 250 μL of a 32 μg/mL material stock corresponds to nominal final material concentrations of 4 or 8 μg/mL, respectively, and a nominal bacterial concentration of 10^6 CFU/mL. The plate-assay concentrations were 4 μg/mL for *E. coli* and MRSA and 8 μg/mL for *S. aureus*. Following treatment, samples were diluted 1000-fold and 100 μL was plated for subsequent colony observation.

The ZAZ stock was described as 3.2 mg material dispersed in 100 mL saline, sonicated for 5 min, and sterilized at 121°C for 15 min.

2.5 Broth assays and bactericidal assessment

The tabulated broth assay combined 100 μL bacterial suspension with 100 μL material-containing medium in each well. If the bacterial suspension contained 10^6 CFU/mL before mixing, its nominal final concentration was 5×10^5 CFU/mL. The concentration labels were 1, 2, 4, and 8 μg/mL for *E. coli* and 1, 2, 4, 8, and 16 μg/mL for *S. aureus* and MRSA. Following incubation at 37°C for 18–24 h, optical density was measured at 620 nm. Selected wells were subsequently plated to assess bacterial recovery. Antibacterial ability is calculated as the number of colonies according to the formula. Colony count $(\frac{CFU}{ml})= \frac{C}{V}\times$M, where C indicates the average number of colonies growing on the plate at a given dilution, V indicates the volume of diluent used to coat the plate (ml), and M indicates the dilution multiple. The MIC value was determined as the lowest concentration of the drug that showed no significant difference in absorbance compared to the control group. The minimum bactericidal concentration (MBC) value is determined by plating the liquid from wells with MIC values and higher concentrations, where the value corresponding to almost no bacterial growth is identified as the MBC.

2.6 MRSA-inoculated wound model and treatment

SD rats underwent isoflurane anesthesia and dorsal hair removal. Two approximately 1 cm-diameter full-thickness wounds were created on opposite sides of the spine. The record describes local use of approximately 0.8 mL lidocaine solution and application of 10 μL MRSA suspension at 10^6 CFU/mL, followed by wound coverage. Wounds were assessed after 24 h for redness, swelling, and purulent appearance as clinical signs of infection. 24 hours after model establishment, the rats confirmed to be successfully infected were divided into three groups. Animals were assigned to saline-loaded dressing (Control group), ZAZ-loaded dressing (ZAZ group) and untreated groups (normal group), with three rats reported per

group. ZAZ suspension was prepared at 4 μg/mL. Dressings were applied on days 1, 3, 6, and 9.

2.7 Tissue assessment and analysis

Wound photography was scheduled for days 0, 1, 3, 6, 9, and 14. On day 14, wound tissue was assessed using hematoxylin and eosin (H&E) and Masson's trichrome staining. Body weight was recorded during follow-up. On the 14th day, the skin around the wound of each rat was collected for HE staining and Masson staining. HE staining is used to evaluate wound recovery, such as structural integrity, epidermal regeneration, and the degree of inflammatory cell infiltration. Masson staining is used to evaluate the level of collagen deposition, which reflects the degree of wound repair from another perspective. Wound area and tissue measurements were described as analyzed using ImageJ, Origin, and SPSS. On day 14, the livers and kidneys of the administration group and the free group were collected for HE staining for biological safety evaluation.

3 Results

3.1 Morphology and composition

SEM showed polyhedral ZIF-8 particles and a change toward a more rounded morphology after AgNO3 treatment (Fig. 1). The initial description estimated particle sizes of approximately 500 nm and 300 nm, respectively. The particles on the ZAZ sphere are speculated to be ZnO. The changes in morphology and particle size as well as the formation of the particles can, on one hand, prove the formation of the composite material. TEM showed additional nanoscale features after treatment, and a reported lattice spacing of approximately 0.28 nm was assigned to ZnO. Together, the microscopy, diffraction, and elemental observations support the designation silver-containing ZnO/ZIF-8 composite. The black substance contained in the surface layer of ZnO. It may belong to $HAg(MI)_2$ and forms together with ZnO (Fig.2). From the TEM image, we can draw the conclusion that ZAZ has a ZIF-8 structure wrapped by ZnO, and the Ag element is successfully doped into it.

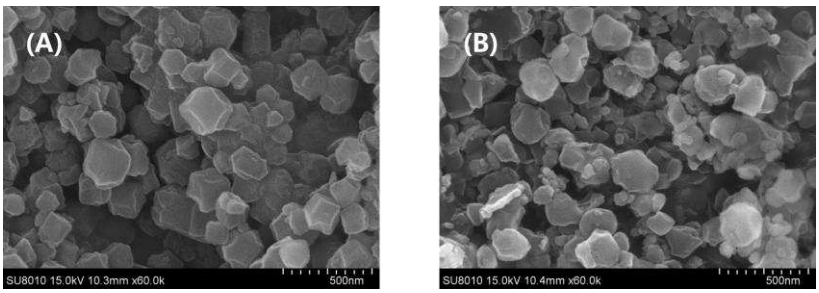

Fig.1 SEM image: (A) ZIF-8, (B) ZAZ

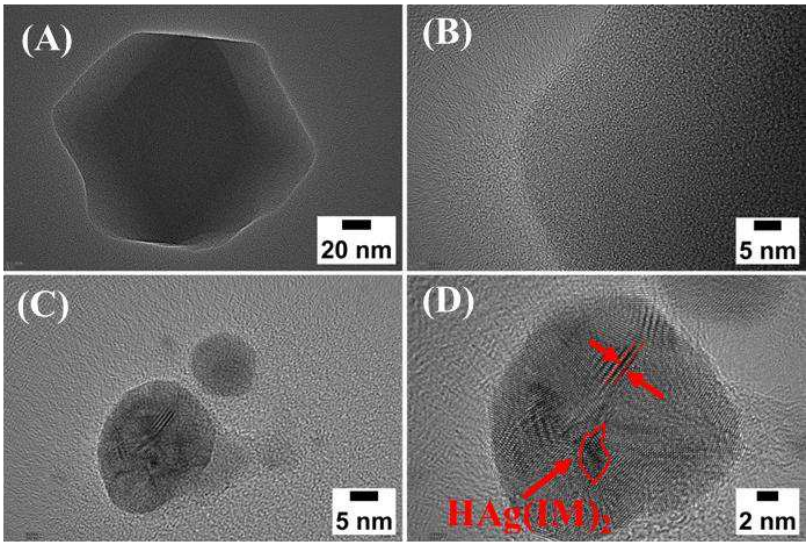

Fig.2 TEM image (A: ZIF-8; B: ZAZ; C: ZIF-8 (High resolution); D:ZAZ (High resolution)

The crystal phases of ZIF-8 and ZAZ were detected by XRD, and the diffraction peaks were assigned. As shown in Fig.3, the peaks appearing at 7.38°, 10.42°, 12.77°, 14.75°, 16.50°, 18.08° and 19.53° are attributed to the (011), (002), (112), (022), (013), (222) and (123) reflections of ZIF-8. New peaks appear at 31.77°, 34.42° and 36.25°, which are attributed to the (100), (002) and (101) reflections of ZnO, respectively. New peaks also appear at 9.08°, 16.94°, 22.49°, 28.01° and 28.53°. These are the diffraction peaks of the $HAg(IM)_2$ complex. $HAg(IM)_2$ represents any silver species linearly coordinated via IM, including polymer complexes as well. From the XRD results, we can analyze and conclude that the as-prepared ZAZ contains ZIF-8, Ag complexes and ZnO, which strongly proves the successful formation of the composite and is consistent with the results obtained from TEM.

EDS was used to analyze the element distribution of ZAZ. The EDS results in Fig.4 indicate that the prepared ZAZ NPs contain five elements: Zn, C, O, N and Ag. Among them, Zn and O elements belong to ZnO or ZIF-8, C and N elements belong to ZIF-8, and Ag element belongs to silver complexes. The EDS results show that the five elements are uniformly distributed in the prepared ZAZ NPs, which proves the successful synthesis of the composite.

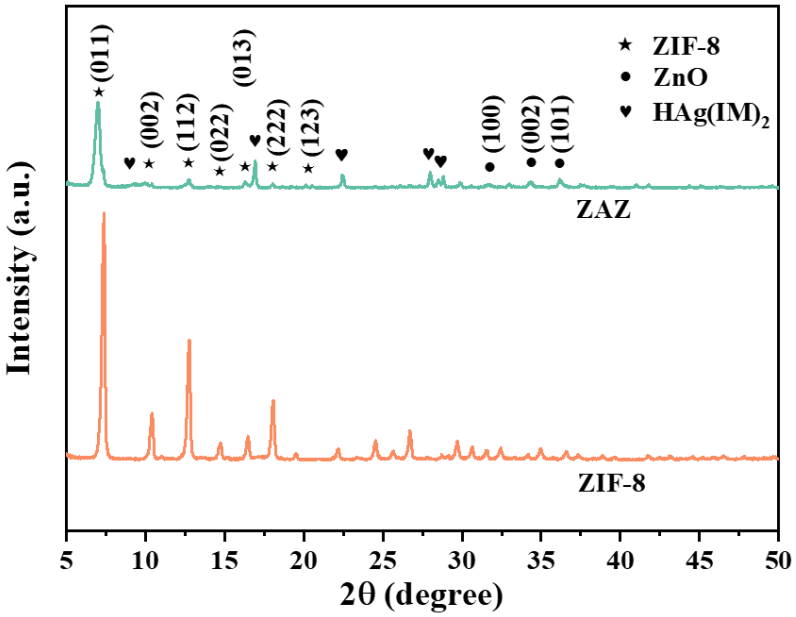

Fig.3 XRD image of ZIF-8 and ZAZ

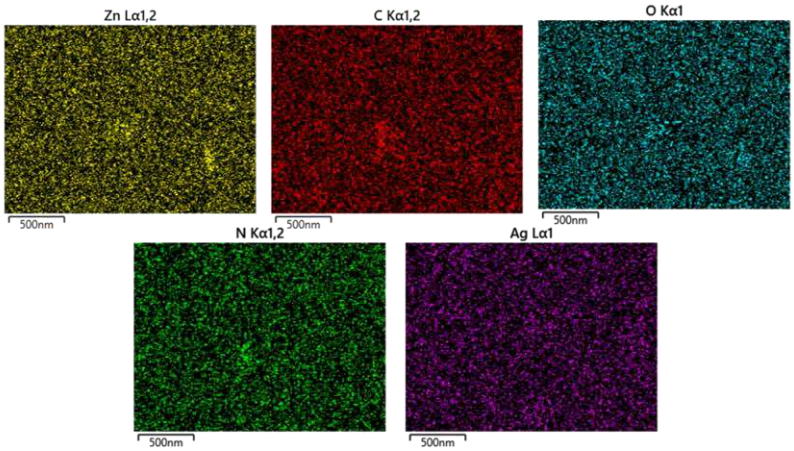

Fig.4 EDS analysis of ZAZ

3.2 Surface chemistry and filtrate elemental concentrations

XPS was used to analyze the elemental composition and chemical valence states of ZAZ. The peaks corresponding to the N and Zn elements of ZIF-8 and ZAZ did not shift, which is because ZAZ is formed via in-situ transformation on the basis of Zn^{2+} on the surface of ZIF-8 (Fig.5). The peaks at 532.9 eV and 531.8 eV corresponding to the O element are attributed to adsorbed oxygen and defect oxygen, respectively, both of which can be ascribed to ZIF-8. The peaks at 532.3 eV, 531.3 eV and 530.3 eV of the O element in ZAZ correspond to adsorbed oxygen, defect oxygen and lattice oxygen, respectively. Among them, adsorbed oxygen and defect oxygen are ascribed to ZIF-8, while lattice oxygen is attributed to ZnO, which also proves the successful formation of ZnO in ZAZ from another aspect. In addition,

two peaks appeared in the Ag element spectrum of ZAZ, which also confirmed the existence of silver complexes in XRD, consistent with the results of XRD and TEM (Fig.6).

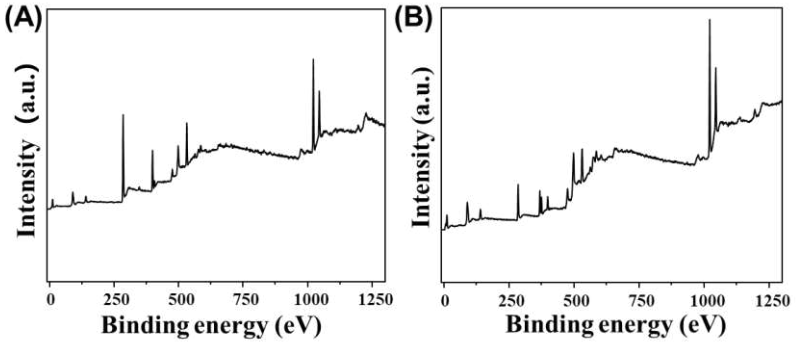

Fig.5 XPS image: (A) ZIF-8, (B) ZAZ

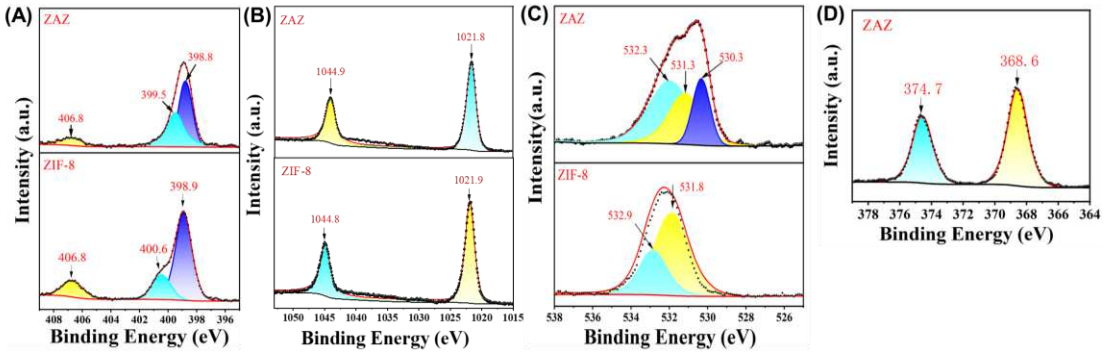

Fig.6 High-resolution XPS spectra of ZIF-8 and ZAZ(A:N; B:Zn; C:O; D:Ag)

Infrared spectroscopy results show that all prepared samples exhibit vibrational bands at 421,759,1145,1306,1457, and 1584 cm^{-1} (Fig.7). The vibrational bands at 421 and 1584 cm^{-1} correspond to the stretching vibrations of Zn-N and C-N bonds, respectively. The peaks at 759 and 1306 cm^{-1} correspond to bending modes of the imidazole ring. The peak at 1457 cm^{-1} corresponds to the stretching vibration of the imidazole ring. The peaks at 2927 and 3133 cm^{-1} are assigned, respectively, to the stretching vibrations of aromatic and aliphatic C-H bonds. These peaks indicate the presence of the ZIF-8 structure in the synthesized material. Upon treatment of ZIF-8 with $AgNO_3$, a new vibrational band appears at 470 cm^{-1}, which is attributed to the stretching vibration of Zn-O. This indicates the formation of ZnO within ZAZ, consistent with the characterization results described above.

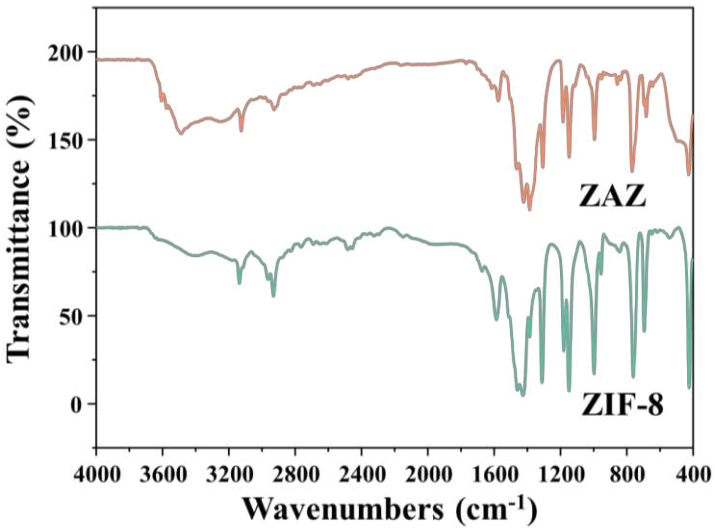

Fig.7 Infrared result images of ZIF-8 and ZAZ

Quantitative detection of the released Zn^{2+} and Ag^{+} from ZAZ NPs in physiological saline at time points 0, 2, 4, 8, and 24 h was performed using inductively coupled plasma optical emission spectroscopy (Fig.8). As time progressed, the amount of Zn^{2+} released by ZAZ peaked at 24 h, exhibiting a steady upward trend during this period, whereas the release of Ag^{+} remained stable throughout. The experimental results demonstrate that the two antibacterial ions can achieve synergistic release in a neutral environment (physiological saline), indicating good antibacterial potential and providing a foundation for in vitro antibacterial studies.

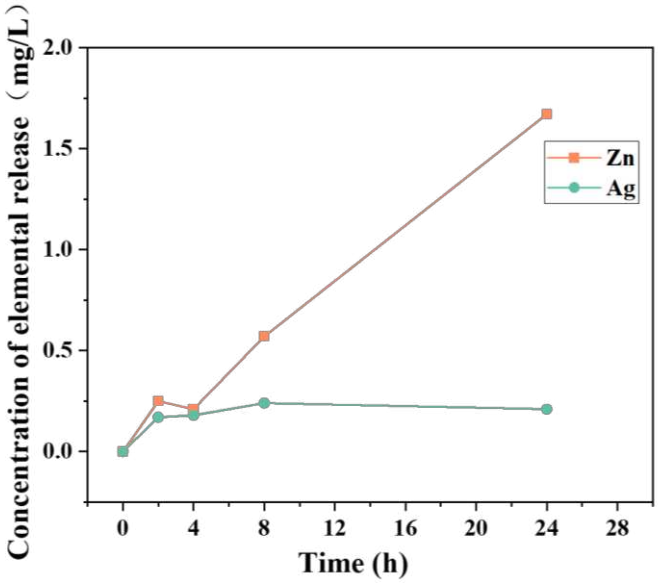

Fig.8 ZAZ releases bivalent metal ions over time

3.3 Antibacterial observations

The agar plate method was used to evaluate the in vitro antibacterial effect of ZAZ NPs. The results showed that at the concentration of 4 μg/ml, the bacteriostatic rates of the ZAZ group, ZIF-8 group and ZnO group against Escherichia coli were 100%, 29.99 ± 1.01% and 66.76 ± 1.99%, respectively (Fig.9). At the concentration of 8 μg/ml, the bacteriostatic rates of the ZAZ group, ZIF-8 group and ZnO group against Staphylococcus aureus were 100%, 67.60 ± 1.01% and 69.89 ± 3.74%, respectively. At the concentration of 4 μg/ml, the bacteriostatic rates of the ZAZ group, ZIF-8 group and ZnO group against MRSA were 100%, 62.82 ±1.63% and 69.75 ± 2.33%, respectively. The antibacterial activity observed from the results of the agar plate counting method can be attributed to the release of bactericidal Zn^{2+} and Ag^{+}. Compared with the ZIF-8 and ZnO groups, the inhibition rate of ZAZ is significantly higher. This is because Ag^{+} and Zn^{2+} released by ZAZ NPs can destroy the ionic environment of bacteria, disrupt the environmental ionic balance, and interfere with ion channels in the cell membrane. They interact with a variety of membrane components, penetrate bacterial cells, damage enzymes, and ultimately lead to bacterial death.

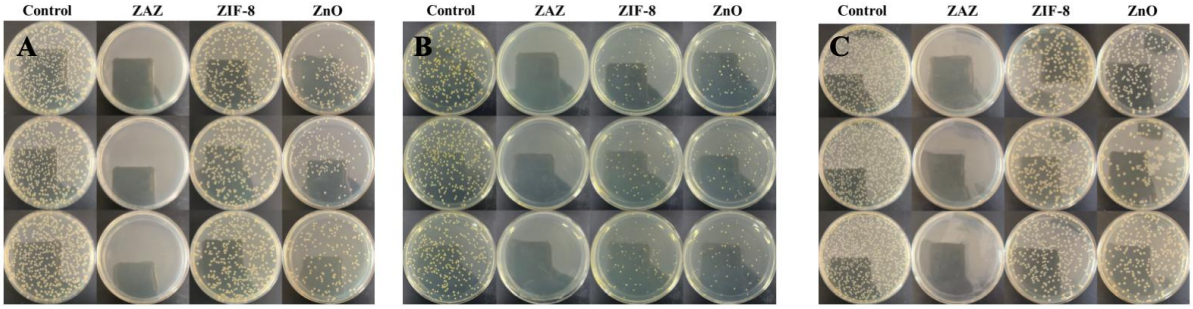

Fig.9 Bacteriostatic effect of ZAZ, ZIF-8 and ZnO (A: Escherichia coli, B: Staphylococcus aureus, C: MRSA)

The results show that the MIC and MBC values of ZAZ NPs against Escherichia coli are 4 μg/mL and 8 μg/mL respectively, and the MIC and MBC values against Staphylococcus aureus and MRSA are 8 μg/mL and 16 μg/mL respectively (Fig.10). These results indicated that ZAZ NPs can effectively inhibit and kill high concentrations of bacteria at low concentrations, exhibiting excellent broad-spectrum antibacterial properties.

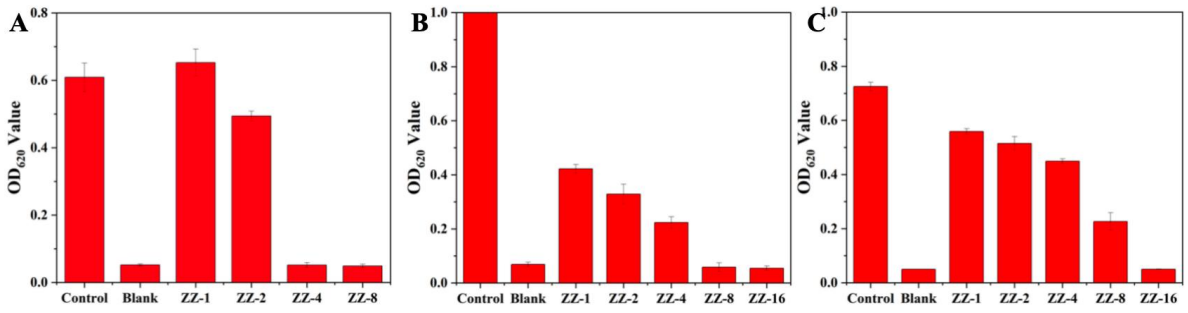

Fig.10 MIC values of ZAZ against different bacteria (A: Escherichia coli, B: Staphylococcus aureus, C: MRSA)

3.4 Evaluation of in vivo antibacterial effect

3.4.1 Wound recovery status

Wound photographs and the area curve showed progressive closure in the ZAZ-treated group. The closure values on day 14 were recorded as 92.04% for the ZAZ group and 72.61% for the control group, which showed a significant difference (Fig.11-12).

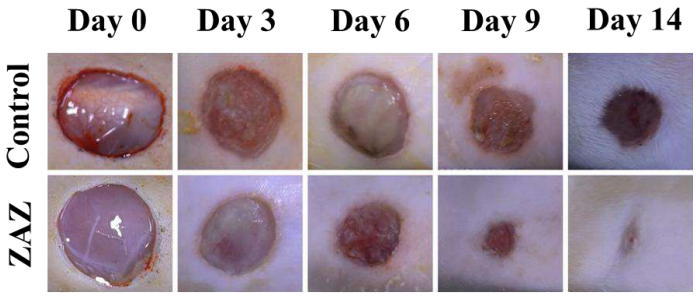

Fig.11 Changes in infected wounds during treatment

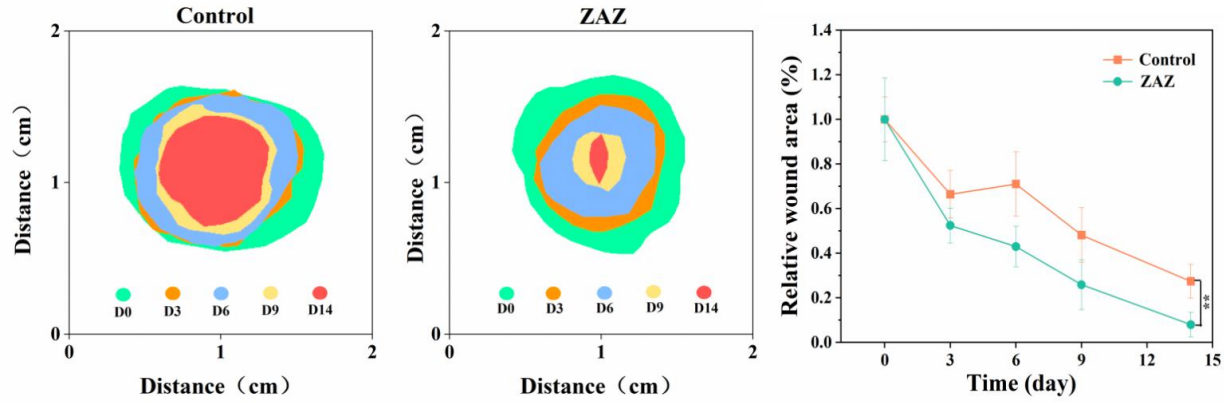

Fig.12 Graph of wound area changes over time

3.4.2 Pathological analysis

The HE staining results showed that inflammatory cell infiltration was present in the control group, while almost no inflammatory cell infiltration was observed in the ZAZ group, and the wound gap in the ZAZ group was significantly smaller than that in the control group (Fig.13). In addition, continuous regenerated epidermis was observed in the ZAZ group, while the regenerated epidermis in the control group was discontinuous, with persistent wound layer defects. Quantitative analysis of the thickness of the regenerated epidermis showed that the epidermal regeneration in the ZAZ group was better than that in the control group, and there was no obvious tendency for scar formation.

To further study the effect of ZAZ in wound antibacterial treatment, the skin tissue around the wound was collected on the 14th day for Masson staining. The results of Masson staining showed that the collagen deposition at the wound site in the ZAZ group was significantly higher than that in the control group (Fig.14). The significant difference in collagen deposition reflects the degree and changes of wound healing from another aspect. In addition, intact skin structures (from bottom to top are the muscle layer, fascia layer, epidermis layer and dermis layer) were also observed in the ZAZ group, which further reflects that the wound repair is in good condition.

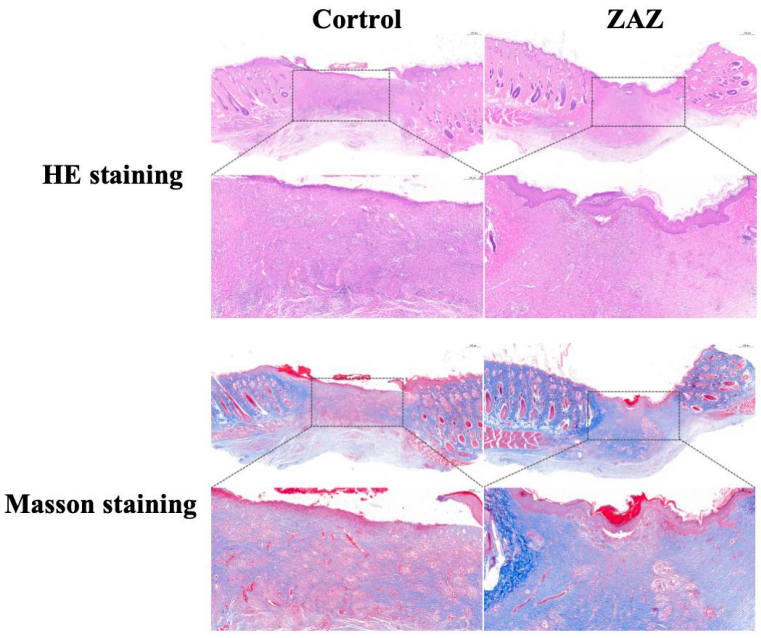

Fig.13 HE staining and Masson staining of skin tissue around the wound

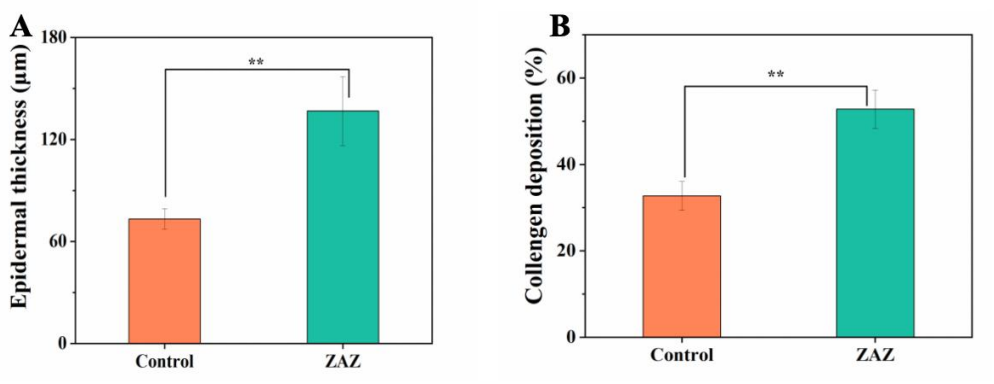

Fig.14 Quantitative analysis results of epidermal thickness (A: HE staining, B: Masson staining)

3.4.3 Biocompatibility evaluation

To further evaluate biological safety, an in vivo biocompatibility assessment was performed on the ZAZ group after 14 days of treatment. Histopathological images of the metabolic organs (liver and kidney) of the infected or treated mice showed no obvious damage after treatment (Fig.15). The results indicate that ZAZ nanoparticles not only achieve rapid and safe wound sterilization and promote wound healing, but also exhibit good biocompatibility.

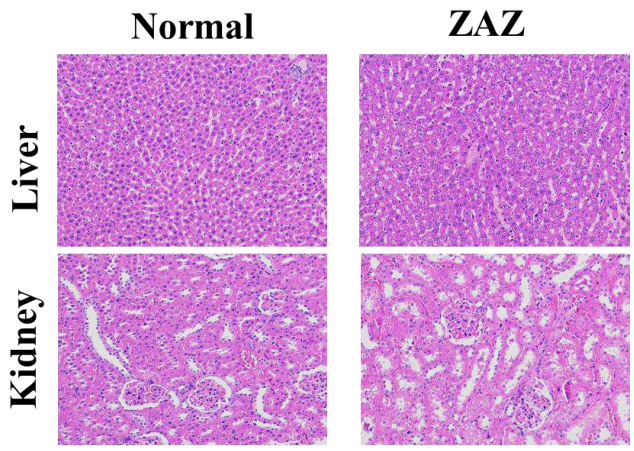

Fig.15 HE staining of liver and kidney

4 Discussion

The widespread spread of antibiotic-resistant bacteria has posed a major challenge to the global public health field, and there is an urgent need to develop new antibacterial agents to address this threat. Against this background, metal-organic framework (MOFs) materials have demonstrated significant application potential in the antibacterial field due to their unique structural characteristics, high specific surface area and tunable functions [26, 27]. Zeolitic imidazolate framework-8 (ZIF-8) has become a hot material in antibacterial research due to its unique structure and properties [28, 29]. Its antibacterial mechanism mainly relies on the controlled release of zinc ions, but there are two notable limitations. Firstly, the antibacterial spectrum of single zinc ions is relatively narrow, making it difficult to meet the challenge of multidrug-resistant strains. Furthermore, the release behavior of Zn^{2+} is pH-dependent and can only be effectively released in acidic environments, which limits its application in physiological environments [30].

This study successfully developed a ZnO@Ag-ZIF-8 nanoparticle (ZAZ NPs) based on the bimetallic ion co-release mechanism. The material was synthesized via the solvothermal method and in-situ transformation method, and exhibits excellent antibacterial properties. Characterization methods including scanning electron microscopy (SEM), transmission electron microscopy (TEM), and X-ray diffraction (XRD) confirmed the structural and morphological features of ZAZ NPs. It not only retains the crystalline structure of ZIF-8, but also successfully introduces silver element, forming a composite structure of ZnO and $HAg(IM)_2$ complex. The results of inductively coupled plasma optical emission spectrometry (ICP-OES) show that ZAZ NPs can effectively release Zn^{2+} and Ag^{+} in a neutral environment, possessing good antibacterial potential.

In vitro experiments demonstrate that ZAZ NPs exhibit significant antibacterial activity against methicillin-resistant Staphylococcus aureus (MRSA), Staphylococcus aureus and Escherichia coli. At low concentrations (4-16 μg/mL), they can effectively inhibit and kill high concentrations of bacteria, with a bacteriostatic rate as high as 100%. Compared with single ZIF-8 and ZnO, the antibacterial effect of ZAZ NPs is significantly enhanced, which is attributed to the fact that the released $Zn^{2+}$and Ag^{+} can synergistically disrupt the ionic environment of bacteria, interfere with cell membrane function, and ultimately lead to bacterial death. By establishing a full-thickness skin wound model in rats infected with MRSA, in vivo experiments further verified the antibacterial and healing-promoting effects of ZAZ NPs. The experimental results show that the wound closure rate of the ZAZ NPs treatment group is significantly higher than that of the control group, and the inflammatory

response is significantly alleviated. Histopathological analysis indicates that ZAZ NPs can promote epidermal regeneration and collagen deposition, accelerating the wound healing process. In addition, biocompatibility tests confirm that ZAZ NPs have no obvious toxicity to liver and kidney tissues, showing good biosafety. These results suggest that ZAZ NPs, through the synergistic effect of bimetallic ions, exhibit highly efficient antibacterial activity and healing-promoting ability, providing a new solution to address the problem of antibiotic resistance.

5 Conclusion

This study successfully developed a ZnO@Ag-ZIF-8 nanoparticle (ZAZ NPs) based on the synergistic effect of bimetallic ions, which exhibits significant advantages in antibacterial properties and wound healing. This study provides a new idea for the development of novel antibacterial materials and a feasible solution to address the problem of antibiotic resistance. Future research can further explore the clinical application potential and long-term biocompatibility of ZAZ NPs, so as to provide more experimental evidence for the development and application of antibacterial materials.

Acknowledgments

This work is supported by Natural Science Foundation of Liaoning Province(2024-MS-004).

Statements and declarations

The authors declare no conflicts of interest.

References

1. Ding X, Tang Q, Xu Z, et al. Challenges and innovations in treating chronic and acute wound infections: from basic science to clinical practice. Burns & Trauma, 2022, 10: tkac014.

2. Wilkinson H N, Hardman M J. Wound healing: cellular mechanisms and pathological outcomes. Open biology, 2020, 10 (9) : 200223.

3. Gupta A. Chapter 1-Fundamentals of skin wound healing and repair: a brief review on cellular and molecular pathophysiologic basis of wound healing. Elsevier, 2022: 1-18.

4. Vivcharenko V, Trzaskowska M, Przekora A, et al. Wound dressing modifications for accelerated healing of infected wounds. International Journal of Molecular Sciences, 2023, 24 (8) : 7193-7220.

5. Gompelman M, Vanasten S A V, Peters E J G, et al. Update on the role of infection and biofilms in wound healing: pathophysiology and treatment. Plastic and Reconstructive Surgery, 2016, 138 (3S) : 61S-70S.

6. Bigham A, Islami N, Khosravi A, et al. MOFs and MOF-based composites as next-generation materials for wound healing and dressings. Small, 2024, 20 (30) : 2311903.

7. Sandar W P, Saw S, Kumar A M V, et al. Wounds, antimicrobial resistance and challenges of implementing a surveillance system in myanmar: a mixed-methods study. Tropical Medicine and Infectious Disease, 2021, 6 (2) :80-95.

8. GBD 2021 Antimicrobial Resistance Collaborators. Global burden of bacterial antimicrobial resistance 1990–2021: a systematic analysis with forecasts to 2050. Lancet. 2024;404:1199–1226. https://doi.org/10.1016/S0140-6736(24)01867-1

9. Cieplik, F.; Deng, D.; Crielaard, W.; et al. Antimicrobial photodynamic therapy: what we know and what we don't. Crit. Rev. Microbiol. 2018, 44, 571-589.

10. Laxminarayan, R.; Matsoso, P.; Pant, S.; et al. Access to effective antimicrobials: a worldwide challenge. Lancet 2016, 387, 168-175.

11. Holmes, A. H.; Moore, L. S.; Sundsfjord, A.; et al. Understanding the mechanisms and drivers of antimicrobial resistance. Lancet 2016, 387, 176-187.

12. Li, X.; Bai, H.; Yang, Y.; Yoon, J.; Wang, S.; Zhang, X. Supramolecular antibacterial materials for combatting antibiotic resistance. Adv. Mater. 2019, 31, 1805092.

13. Guo Z, Xiao Y, Wu W, et al. Metal-organic framework-based smart stimuli-responsive drug delivery systems for cancer therapy: advances, challenges, and future perspectives[J]. Nanobiotechnology, 2025, 23 (1) : 157-200.

14. Murtaza G, Ahmed M I, Yu K, et al. Challenges and outlooks for the polyoxometalates, metal-organic frameworks (POMs-MOFs) hybrid materials in water treatment technologies. Environmental Research, 2025, 272 : 121156.

15. Fatah S A, Omer K M. Aptamer-modified MOFs (Aptamer@MOF) for efficient detection of bacterial pathogens: a review. ACS Applied Materials & Interfaces, 2025, 17 (8) : 11578-11594.

16. Ahmadi M, Ayyoubzadeh S M, Ghorbani-bidkorbeh F, et al. An investigation of affecting factors on MOF characteristics for biomedical applications: a systematic review. Heliyon, 2021, 7 (4) : e06914.

17. Monika P, Chandraprabha M N, Rangarajan A, et al. Challenges in healing wound: role of complementary and alternative medicine. Frontiers in Nutrition, 2022, 8 : 791899.

18. Liu Y, Jiang T, Liu Z, et al. Metal-organic frameworks for bioimaging: strategies and challenges. Nanotheranostics, 2022, 6 (2) : 143-160.

19. Han G, Ceilley R. Chronic wound healing: a review of current management and treatments[J]. Advances in Therapy, 2017, 34 (3) : 599-610.

20. Fatah S A, Omer K. Aptamer-modified MOFs (Aptamer@MOF) for efficient detection of bacterial pathogens: a review. ACS Applied Materials, 2025, 17 (8) : 11578-11594.

21. Lu X, Ye J, Zhang D, et al. Silver carboxylate metal–organic frameworks with highly antibacterial activity and biocompatibility. Journal of Inorganic Biochemistry, 2014, 138: 114-121.

22. Berchel M, Gall T L, Denis C, et al. A silver-based metal–organic framework material as a "reservoir" of bactericidal metal ions. New Journal of Chemistry, 2011, 35 (5) : 1000-1003.

23. Yang Y, Wu X, He C, et al. Metal-organic framework/Ag-based hybrid nanoagents for rapid and synergistic bacterial eradication. ACS Applied Materials & Interfaces, 2020, 12 (12) : 13698-13708.

24. Li P, Li J, Feng X, et al. Metal-organic frameworks with photocatalytic bactericidal activity for integrated air cleaning. Nature Communications, 2019, 10 (1) : 2177-2187.

25. Godakhindi V, Kravitz E, Vivero-escoto J L, et al. Light-activable silver nanoparticles for combatting antibiotic-resistant bacteria and biofilms. Molecules, 2025, 30 (3) : 626-643.

26. Esfahanian M, Ghasemzadeh M A, Razavian S M H, et al. Synthesis, identification and application of the novel metal-organic framework Fe3O4@PAA@ZIF-8 for the drug delivery of ciprofloxacin and investigation of antibacterial activity. Artificial Cells Nanomedicine and Biotechnology, 2019, 47 (1) : 2024-2030.

27. Mao D, Hu F, Kenry, et al. Metal-organic-framework-assisted in vivo bacterial metabolic labeling and precise antibacterial therapy. Advanced Materials, 2018, 30 (18) : e1706831.

28. Li P, Li J, Feng X, et al. Metal-organic frameworks with photocatalytic bactericidal activity for integrated air cleaning. Nature Communications, 2019, 10 (1) : 2177-2187.

29. Yang Y, Wu X, He C, et al. Metal-organic framework/Ag-based hybrid nanoagents for rapid and synergistic bacterial eradication. ACS Applied Materials & Interfaces, 2020, 12 (12) : 13698-13708.

30. Nabipour H, Soltani B, Ahmadi N, et al. Gentamicin loaded $Zn_2(bdc)_2(dabco)$ frameworks as efficient materials for drug delivery and antibacterial activity. Journal of Inorganic and Organometallic Polymers and Materials, 2018, 28 (3) : 1206-1213.